IPEM
Institute of Physics and
Engineering in Medicine

Simulation-based evaluation and optimization of a new CdZnTe gamma-camera architecture (HiSens)

To cite this article: Charlotte Robert *et al* 2010 *Phys. Med. Biol.* **55** 2709

View the article online for updates and enhancements.

You may also like

- Characterization of a sub-assembly of 3D position sensitive cadmium zinc telluride detectors and electronics from a sub-millimeter resolution PET system
Shiva Abbaszadeh, Yi Gu, Paul D Reynolds et al.

- Tilted angle CZT detector for photon counting/energy weighting x-ray and CT imaging
Polad M Shikhaliev

- ASTROSAT CZT IMAGER OBSERVATIONS OF GRB 151006A: TIMING, SPECTROSCOPY, AND POLARIZATION STUDY
A. R. Rao, Vikas Chand, M. K. Hingar et al.

Recent citations

- Evaluation of a variableaperture fullring SPECT system using largearea pixelated CZT modules: A simulation study for brain SPECT applications
Yoonsuk Huh *et al*

- Technical Note: Nuclear imaging with an x ray flat panel detector: A proofofconcept study
Martijn M. A. Dietze *et al*

- Conceptual design of a large pixelated CZT detector with four-hole collimator matched pixel detector for SPECT imaging: a Monte Carlo simulation study
N. Boutaghane *et al*
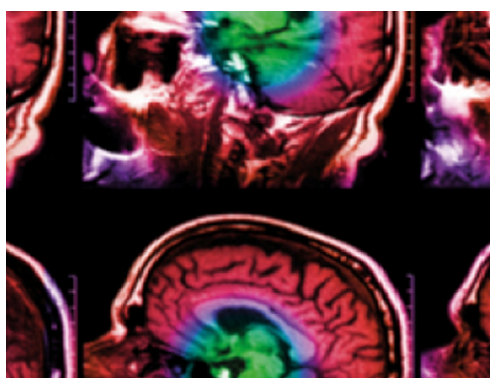
IPEM | IOP
Series in Physics and Engineering in Medicine and Biology

Your publishing choice in medical physics, biomedical engineering and related subjects.

Start exploring the collection—download the first chapter of every title for free.

Simulation-based evaluation and optimization of a new CdZnTe gamma-camera architecture (HiSens)

Charlotte Robert[1]**, Guillaume Montémont**[1]**, Véronique Rebuffel**[1]**, Irène Buvat**[2]**, Lucie Guérin**[1] **and Loïck Verger**[1]

[1] CEA, LETI, MINATEC, F38054 Grenoble, France
[2] IMNC—UMR 8165 CNRS, Universités Paris 7 et Paris 11, Bât 104, 91406 Orsay, France

Abstract

A new gamma-camera architecture named HiSens is presented and evaluated. It consists of a parallel hole collimator, a pixelated CdZnTe (CZT) detector associated with specific electronics for 3D localization and dedicated reconstruction algorithms. To gain in efficiency, a high aperture collimator is used. The spatial resolution is preserved thanks to accurate 3D localization of the interactions inside the detector based on a fine sampling of the CZT detector and on the depth of interaction information. The performance of this architecture is characterized using Monte Carlo simulations in both planar and tomographic modes. Detective quantum efficiency (DQE) computations are then used to optimize the collimator aperture. In planar mode, the simulations show that the fine CZT detector pixelization increases the system sensitivity by 2 compared to a standard Anger camera without loss in spatial resolution. These results are then validated against experimental data. In SPECT, Monte Carlo simulations confirm the merits of the HiSens architecture observed in planar imaging.

(Some figures in this article are in colour only in the electronic version)

1. Introduction

Single photon emission imaging is most often based on the Anger camera principle (Anger 1967): a collimator is placed in the front of a NaI(Tl) scintillation crystal associated with a set of photomultipliers. These scintillation detectors have reached their limits (energy resolution of about 9% FWHM at 140 keV and intrinsic spatial resolution of about 3 mm at 140 keV for a 3/8 inch thick NaI crystal). To overcome these limitations, CdTe or CdZnTe (CZT) large field of view gamma cameras (Barber 1999, Eisen 1996, Wagenaar *et al* 2003, Verger *et al* 1997, Verger *et al* 2004) such as PEGASE, NUCAM (Eisen *et al* 2002) or BIOMED (Scheiber and Giakos 2001) have been proposed. They offer a better energy resolution (<3%

FWHM at 140 keV) which enables multi-isotopic imaging, a high intrinsic spatial resolution and a higher count rate due to their pixelated structure and modular electronics. However, as most of them use parallel collimators with classical aperture angles, they are still limited by the same trade-off between spatial resolution and sensitivity as the Anger cameras.

To further improve the performance in gamma imaging using semi-conductor detectors, we propose an innovative approach that consists of a pixelated CZT detector (Gros D'Aillon *et al* 2005) associated with a specific electronics for 3D localization (Montémont *et al* 2008), a high sensitivity collimation geometry and dedicated reconstruction algorithms. The aim of this so-called HiSens architecture (Guérin *et al* 2008) is to reduce the acquisition duration while maintaining the spatial resolution obtained with a standard collimator. To reach this goal, two major characteristics of the CZT detector are used: the fine sampling of the CZT detector and the availability of the depth of interaction (DOI) information. For both planar and SPECT acquisitions, the detected signal is processed using an adapted reconstruction algorithm to produce images of the source object.

In the present study, a complete evaluation of the performance of the HiSens configuration is presented. First, the HiSens principle is described. Next, Monte Carlo simulations of the imaging system are performed to characterize the performance of HiSens in a planar imaging configuration. Experimental data acquired with a small field of view CZT imaging bench are also analyzed to validate the simulations. The collimator aperture is optimized in planar mode based on detective quantum efficiency (DQE) computation. Finally, Monte Carlo simulations of SPECT acquisitions using the proposed system are presented.

2. Background

The HiSens architecture associates four components: a pixelated CZT detector, electronics for 3D localization, a parallel square-hole collimator and a dedicated reconstruction algorithm. To increase the system sensitivity, a high aperture collimator is used. The resulting loss of spatial resolution is compensated by an accurate 3D localization of the photon interactions inside the CZT detector, based on the fine pixelization of the CZT detector and on the DOI information.

The DOI information is obtained using the rise time of the signal (Verger *et al* 2004, Gros D'Aillon *et al* 2005) or the amplitude of the cathode signal (He *et al* 1996). Using the DOI information, the CZT detector is divided in several virtual layers. One image per virtual layer is produced. Each image corresponds to a different angular aperture of the collimator (figure 1) and provides a specific 'view' of the source location.

The fine pixelization of the CZT detector is performed using an electronically based 3D positioning algorithm, based on barycentric localization (Warburton 1997), without an increase of the number of read-out channels. This pixelization finely samples the acquired data using several virtual pixels per collimator hole as shown in figure 2.

Figures 1 and 2 illustrate how the HiSens architecture reduces the back-projection cones compared to conventional architecture.

3. Material and methods

3.1. Simulation-based evaluation of the HiSens architecture for planar imaging

3.1.1. Phantom and simulations. The validation of the HiSens architecture was first performed in planar imaging using a ^{57}Co voxelized thyroid phantom (71 mm $\times$ 59 mm
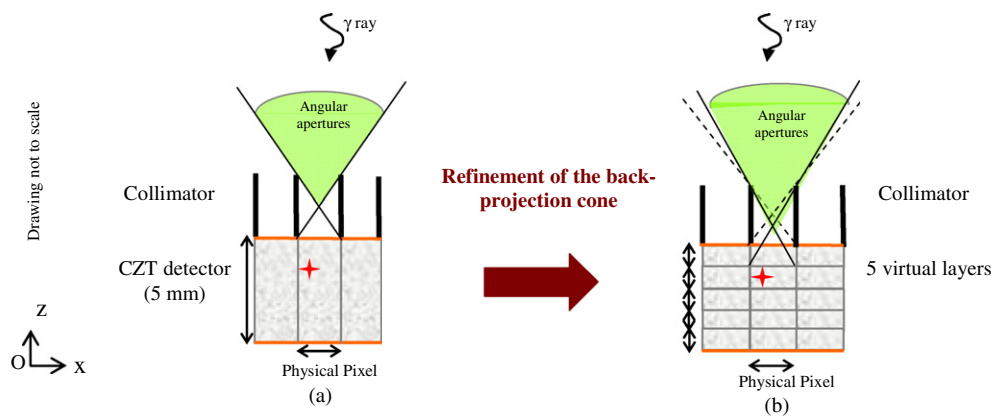
Figure 1. Schemes of the different angular collimator apertures associated with (a) one layer of 5 mm or (b) five layers of CZT detector.
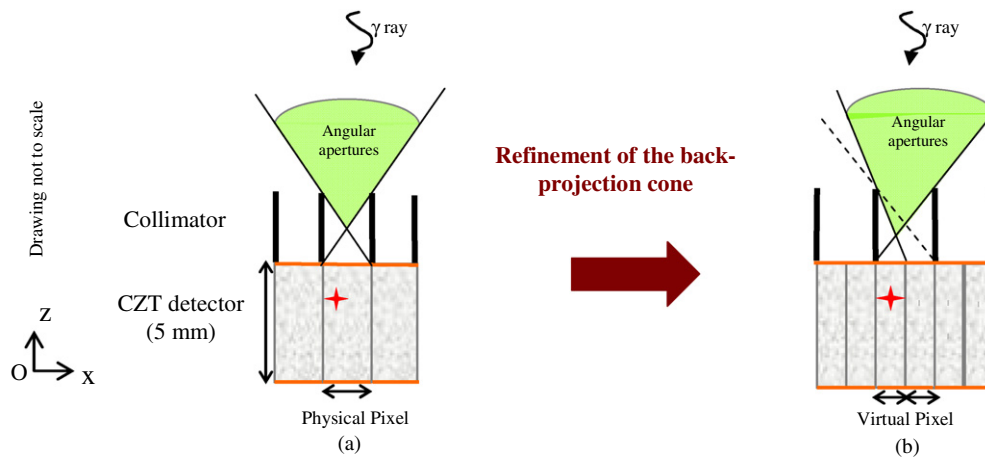

Figure 2. Schemes of the different angular collimator apertures associated with (a) 1 or (b) 4 pixels per collimator hole.
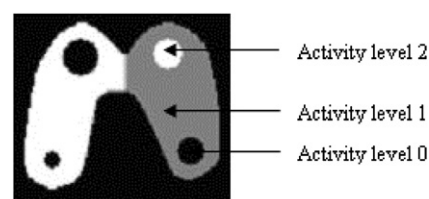

Figure 3. [57]Co voxelized thyroid phantom used for simulation-based study in the planar acquisition mode.

$\times$ 18 mm) that included three cold (6, 11 and 13 mm diameters) and one hot (11 mm diameter) inserts (figure 3).

   Two collimators were considered. The first was a high sensitivity collimator, denoted as H13 hereafter, with the same characteristics as the one available in our lab (1.6 mm collimator

pitch, 13.5 mm septal height and 0.15 mm septal thickness). The second collimator, H29, was a standard LEHR collimator (1.6 mm collimator pitch, 29 mm septal height and 0.15 mm septal thickness). The two collimators had a ratio of about 5 in sensitivity. A 5 mm thick and 211.2 mm × 211.2 mm large (132 × 132 pixels) detector was modelled. Two different pixelizations were investigated: detector pitch equal to 1.6 mm (1 pixel detector per collimator hole) and 0.8 mm (4 virtual pixels per hole). In all configurations, the source to collimator distance was set to 100 mm.

These phantom and detector were modelled using the GATE Monte Carlo simulation tool (Jan *et al* 2004). Photoelectric, Compton and Rayleigh effects were simulated. To model the signal processing steps, the energy deposits by interactions occurring in the same detector pixel were first summed and a Gaussian energy blurring corresponding to a 4% energy resolution at 122 keV was applied. No spatial blurring nor electronic noise was introduced. No charge sharing was simulated. The acquisition duration was set to 283 s for all configurations.

3.1.2. Image reconstruction. With conventional gamma cameras, no reconstruction is performed in planar mode: the projection is directly interpretable. With the HiSens configuration, a collimator response deconvolution must be performed to take advantage of the fine spatial sampling of the projections and to combine images acquired with different angular apertures, such as those provided by each layer and sub-pixel. This deconvolution was performed using an adapted iterative OSEM (ordered subset expectation maximization) reconstruction algorithm (Hudson and Larkin 1994) in which each subset corresponded to the projection acquired for a given depth of interaction. The reconstruction step was always performed even if a single layer was used. Only one subset corresponding to the simulated projection was considered in this case. Two configurations were analyzed: a single 5 mm thick layer (no DOI information) and three virtual layers whose thicknesses were, respectively, equal to 0.8, 1.2 and 3.0 mm to have equivalent efficiencies (the thickness of each layer was set in such a way that layers detected approximately equal numbers of photons). The system matrix modelling the forward and the back-projection steps was calculated using the GATE Monte Carlo simulation tool. About 1.25×10^9 photons were simulated to obtain smoothed matrices. Only the photoelectric effect was modelled here.

3.1.3. Figures of merit. Two figures of merit were used to characterize the reconstructed images: the contrast and the noise. They were estimated on 2D images resulting from the summation along the Z-axis, defined in figure 1, of the reconstructed 3D object. The contrast was defined as

$$C = \frac{(v_1 - v_2)}{(v_1 + v_2)} \times 100, \tag{1}$$

where v_1 and v_2 represent mean level values of 3 × 3 square areas in the hot and cold (right inferior 11 mm diameter cold insert) regions, respectively. For noise assessment, a variance image corresponding to high frequency noise was calculated using

$$\frac{(v_i - m_i)^2}{m_i^2}, \tag{2}$$

where v_i represented the value of pixel i and m_i was the mean value of the eight neighbouring pixels. The mean of the variance image was calculated for all pixels corresponding to uniform areas of the thyroid. This resulting value was easy to calculate from a single noisy projection and shown to nicely correlate with a more accurate noise measure defined from the 20 reconstructions of 20 noisy projections, by considering the average standard deviation
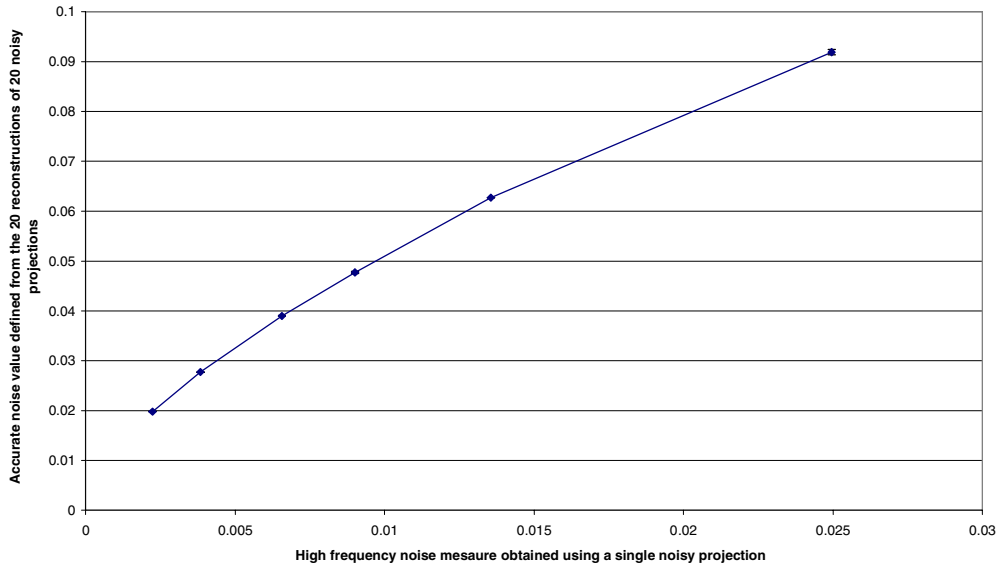
Figure 4. Correlation between the accurate noise measure, defined from 20 reconstructions of 20 noisy projections, and the high frequency noise value, obtained using a single noisy projection and its uncertainties.

over pixels with non-zero values (figure 4). Plots of contrast against noise values were drawn for each configuration (LEHR collimation and H13 collimation with and without DOI and over-pixelization).

3.2. Experimental validation in planar imaging

Experimental planar data were also acquired with the LEHR and the high sensitivity HiSens collimators.

3.2.1. Acquisition set-up. A small field of view gamma imager based on a 4×4 pixel CZT detector MINIGAMI was used (figure 5(a)). A detailed description of this detector and associated electronics can be found in Montémont *et al* (2008). The phantom was the same as the simulated phantom (figure 3). A mechanical translation of the imaging device was used to acquire the entire projections. The LEHR (29 mm high) or high sensitivity H13 square hole parallel collimators (figure 5(b)) were used. Unlike in the simulation, the collimators had only 6×6 holes corresponding to a 9.75 mm $\times$ 9.75 mm area. All acquisitions were performed with one physical pixel per collimator hole. An electronically based 3D positioning algorithm was used to divide the detector in virtual layers and virtual sub-pixels along the *X*- and *Y*-axes (4 pixels per collimator hole).

3.2.2. Data acquisition and reconstruction. For each position of the small imaging device, the acquisition time was set to 170 s which yielded 0.15 detected Mcounts and 0.65 Mcounts using the LEHR and HiSens configurations, respectively. The reconstructions of the thyroid phantom images were performed as previously described (section 3.1.2).
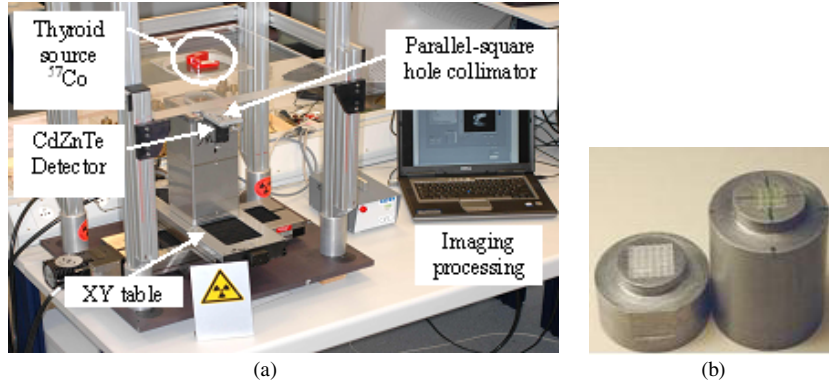
Figure 5. (a) Experimental MINIGAMI set-up. (b) 1.6 mm pitch collimators of 13.5 mm and 29 mm heights.

3.3. Optimization of the collimator aperture

3.3.1. DQE calculation. The initial simulation-based evaluation of the HiSens architecture was performed using the H13 collimator similar to the experimental collimator available in the lab. Then, we optimized the collimator parameters to further improve the spatial resolution, contrast and noise properties of the reconstructed images. The optimized collimator was defined as the one recovering or improving the spatial resolution obtained with the LEHR collimator while maximizing the sensitivity.

To optimize the collimator pitch and septa height, DQE (Cunningham and Shaw 1999) computations were performed. DQE is a figure of merit that takes the spatial resolution and the efficiency into account and also characterizes the useful sensitivity for each spatial frequency. By definition, DQE characterizes the imaging system regardless of the object under investigation. DQE has already been used to compare detection systems including gamma cameras (Starck *et al* 2005). Equation (3) gives the general expression of DQE:

$$\text{DQE}(u, v) = \frac{\text{SNR}(u, v)_{\text{out}}^2}{\text{SNR}(u, v)_{\text{in}}^2}, \tag{3}$$

where u and v are the spatial frequencies in the x and y directions, which are parallel to the detection plan, and SNR_{in} and SNR_{out} are the input and output signal-to-noise ratios, respectively.

In gamma imaging, several hypotheses are used to simplify the DQE expression. As described by Montémont *et al* (2008), a stationary noise, shift invariant by block (i.e. collimator periodicity), should be first considered. Moreover, it should be assumed that the noise affecting the signal is only due to the gamma photon detection statistic. Under these assumptions, for the HiSens configuration in which n sets {virtual layer, sub-pixel} i ($i = 0, \ldots, n-1$) are considered, DQE is given by (Montémont *et al* 2008)

$$\text{DQE} = \sum_{i=0}^{i=n-1} \text{DQE}_i = \sum_{i=0}^{i=n-1} S_i \times \text{MTF}_i^2, \tag{4}$$

where S_i and MTF_i are, respectively, the sensitivity and the module of the normalized modulation transfer function corresponding to {virtual layer, sub-pixel} set i. The MTF was simulated using a ^{57}Co source point. For computational efficiency, the projections of the point sources were simulated using the SINDBAD software (Tabary *et al* 2004) instead of
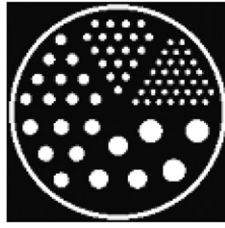
Figure 6. Cold cylindrical phantom including hot inserts (^{57}Co) of increasing size (4, 5.6, 7.2, 10.4, 12.8 and 16 mm) used for assessing the collimator performance in planar imaging.

GATE. SINDBAD performed analytical simulations of the imaging system, ignoring Compton and Rayleigh scattering. The MTFs were deduced from the point spread function (PSF) images using a Fourier transform.

Several collimator geometries were compared. The septal thickness was always set to 0.15 mm and the detector pixel size to 0.8 mm. Two parameters were varied: the collimator hole size varied from 0.8 mm (1 pixel per collimator hole) to 3.2 mm (16 pixels per collimator hole) and the septal height from 5 to 29 mm. In all cases, the source to collimator distance was set to 100 mm. DQE were calculated for each combination for all frequencies of clinical interest (< 1.2 cm^{-1}) (Starck *et al* 2005). This 1.2 cm^{-1} value, which corresponds to about 9 mm spatial resolution, is the present frequency limit of NaI Anger gamma cameras. Lastly, DQE curves corresponding to 5–15 cm source to collimator distances were plotted for the LEHR collimator and the collimator defined as optimal.

3.3.2. Phantoms for collimator optimization. The voxelized thyroid phantom (figure 3) was first used to plot the contrast against noise curve (section 3.1.3) corresponding to the HiSens collimation geometry defined as optimal. A ^{57}Co Derenzo phantom (147.2 mm × 147.2 mm × 38.4 mm) including six areas containing hot inserts in a cold background (4, 5.6, 7.2, 10.4, 12.8 and 16 mm) was also used to visually assess the spatial resolution obtained with the LEHR and the optimized HiSens collimators (figure 6).

As in the previous simulation-based study, projections of the two voxelized phantoms were modelled using GATE to obtain realistic projections including Compton and Rayleigh scatter. In either case, the source to collimator distance was set to 100 mm. The system matrices used for the reconstruction were analytically calculated using SINDBAD.

The high frequency noise (equation (2)) was evaluated using the Derenzo phantom reconstructed images, by considering the inner volumes of the three largest inserts for several iteration numbers. These measurements were used to determine the iteration numbers leading to the same noise level and these numbers of iterations were used to compare the Derenzo reconstructed images.

3.4. Simulation-based evaluation of the HiSens architecture in SPECT

3.4.1. Phantom and simulations. A cylindrical phantom (128 mm diameter, 74.4 mm high), with $0.8 \times 0.8 \times 0.8$ mm^3 voxel size, was used (figure 7). The phantom included two sets (one hot and one cold) of spherical inserts of increasing size (4.8; 5.6; 6.4; 8.0; 9.6; 12.8; 16; 19.2 mm) in an active ^{99m}Tc background, centered in two parallel planes that were 21.6 mm apart. The hot insert to background ratio was set to 4:1.
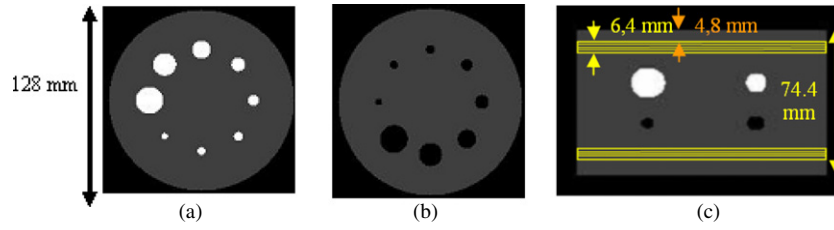
Figure 7. Cylindrical phantom used for evaluation of the HiSens architecture in SPECT. (a) Hot spherical inserts in a ^{99m}Tc background (4.8; 5.6; 6.4; 8.0; 9.6; 12.8; 16 and 19.2 mm) with an insert-to-background ratio set to 4:1. (b) Cold spherical inserts in a ^{99m}Tc background. (c) Localization of the eight planes (4 × 2) used for the assessment of noise in the reconstructed images.

The detector characteristics were the same as those described in section 3.1.1, except for the detector area (312 × 312 mm). To be consistent with a realistic SPECT scan, the radius of rotation was set to 164 mm and 64 projections were acquired over 360°. The source to collimator distance was different from the one simulated in the planar evaluation. Moreover, the rotational motion in SPECT can affect the signal frequency content. Therefore, the optimal collimator for SPECT imaging may not have the same characteristics as the optimal collimator for planar imaging. For this reason, three collimators, the LEHR, the H13 and the optimized one, were modelled using GATE. Finally, acquisitions times were adapted for each collimator to obtain 0.3 Mcounts per view angle.

3.4.2. Image reconstruction. The OSEM algorithm was used for image reconstruction. Projections acquired for each layer and each view angle were used as an input. Depending on the implementation of the DOI information, 16 (1 DOI) or 48 (3 DOI) subsets were used, each containing four orthogonal projections corresponding to a given layer. The system matrices were modelled using the ray-tracing method (SINDBAD software).

3.4.3. Figures of merit. Contrast and noise in the reconstructed images were measured. Contrast was calculated using equation (1) for the five largest hot and cold spherical inserts. The high frequency noise variance image (equation (2)) was calculated for eight parallel planes, located on both sides of the spherical inserts (figure 7(c)), with uniform activity. For each plane, the mean of the variance image was calculated. The noise was defined as the average of the eight values.

4. Results

4.1. Simulation-based evaluation of the HiSens architecture in planar imaging

Figure 8 shows the contrast versus noise curves obtained in planar imaging (GATE simulation-based evaluation). For a given level of noise, contrast is significantly improved by the CZT detector over-pixelization. However, for this configuration, the depth of interaction information (three virtual layers) has no substantial impact. Figure 8 also shows that the contrast/noise trade-off achieved with the H13 collimator associated with the HiSens architecture is worse than the one obtained with the LEHR collimator. Thus, for a gain of acquisition time of five, brought by the H13 collimator compared to the LEHR collimator, the CZT detector over-pixelization improves the contrast/noise trade-off without reaching
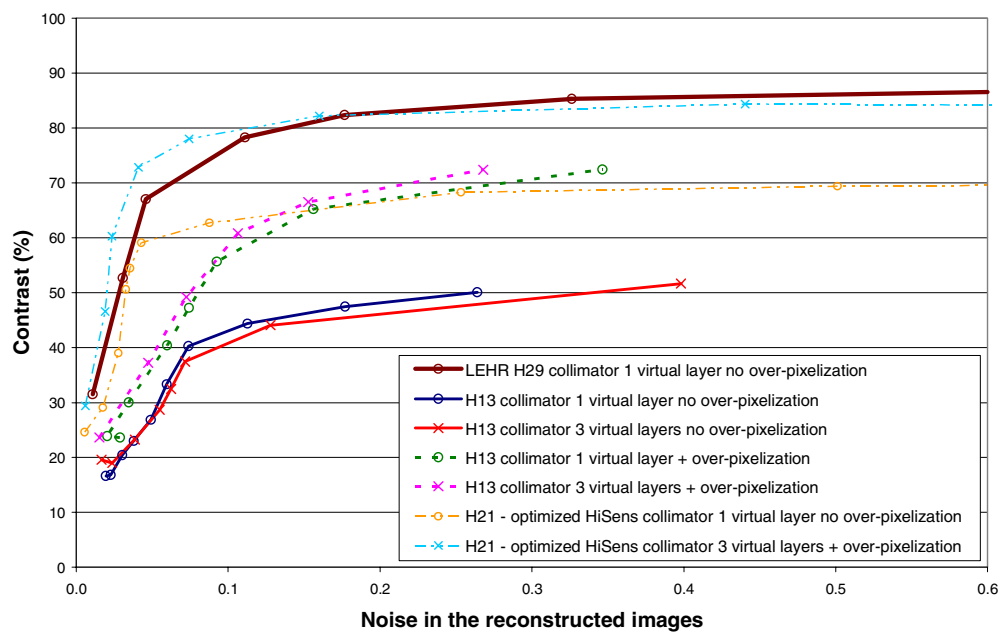
Figure 8. Contrast versus noise curves in the reconstructed images in planar imaging (^{57}Co thyroid source—equivalent times).

Figure 9. Comparison between GATE-simulated and experimental thyroid projections (^{57}Co source). Projections were acquired with the standard LEHR (0.15 Mcounts) and the non-optimized H13 (0.65 Mcounts) collimators.

the LEHR collimator performance. Hence the need to optimize the collimator parameters as shown below.

4.2. Experimental results in planar imaging

GATE-simulated and experimental projections of the thyroid phantom are compared in figure 9, suggesting a reasonable agreement between simulated and real data. Reconstructed images
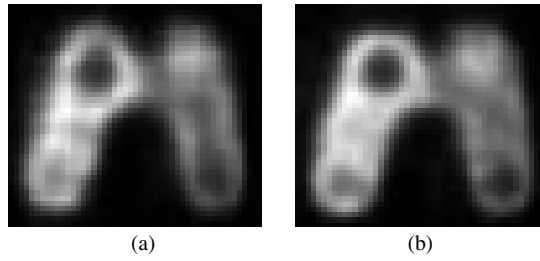
(a)   (b)

Figure 10. Experimental reconstructed images using the H13 collimator with the same noise level (^{57}Co source). (a) One virtual layer/without over-pixelization configuration. (b) Three virtual layers/with over-pixelization configuration. Images are represented using common min. and max. for all images.
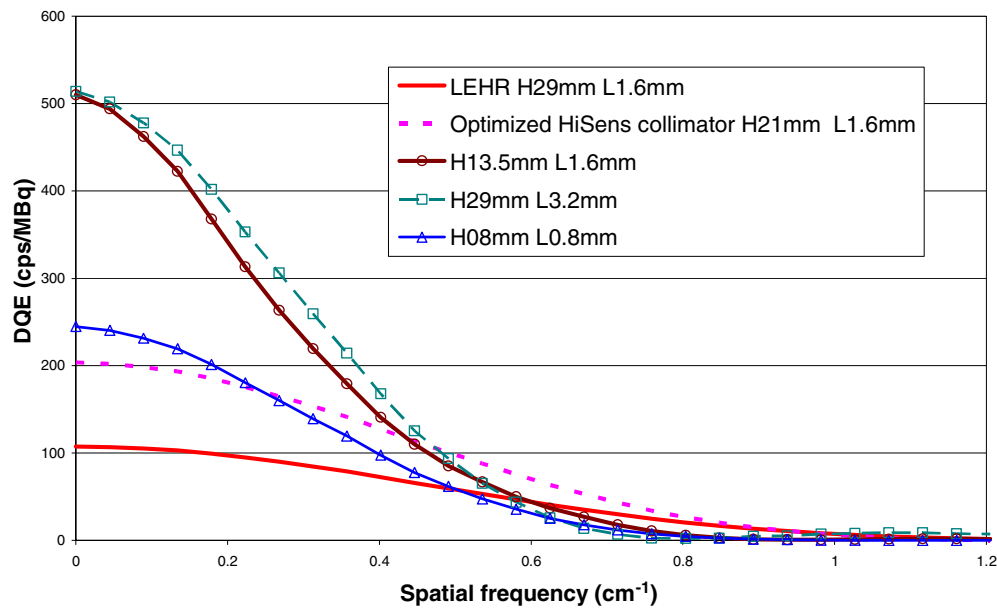

Figure 11. DQE values calculated for a 100 mm source–collimator distance with different collimation architectures (^{57}Co source). In the caption, H corresponds to the septal height of the collimator and L is the pitch.

4.3. Optimization of the collimator aperture

Figure 11 compares the DQE curves corresponding to several collimation configurations for a 100 mm distance between the collimator and the ^{57}Co source. The optimized collimator was defined as that recovering or even improving the DQE curves observed for the reference LEHR collimator for each spatial frequency of interest (equation (5)) with a maximal sensitivity gain (given by DQE(0)) (equation (6)):
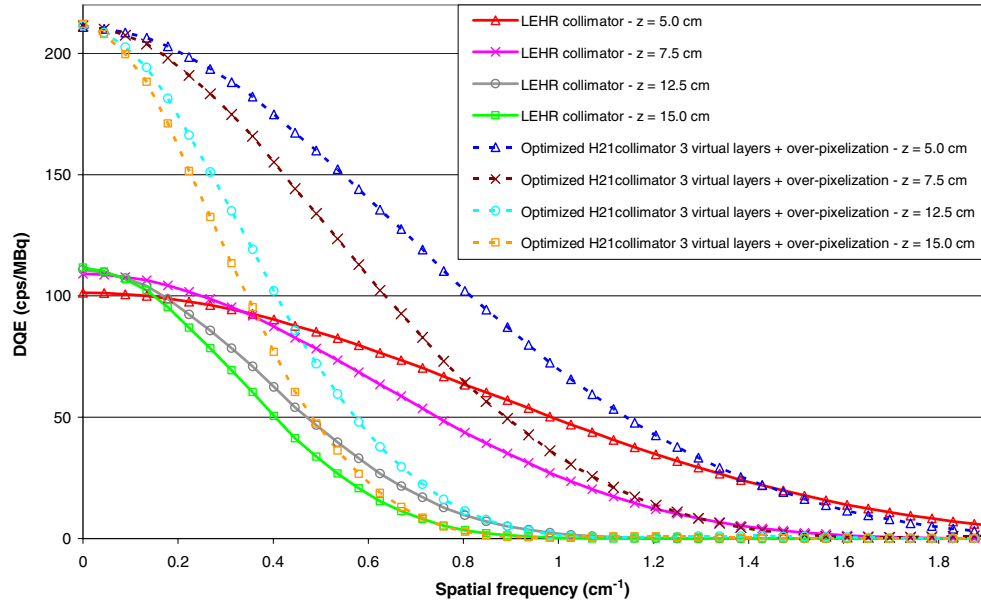
Figure 12. DQE curves obtained with the LEHR and the optimized H21 HiSens (21 mm septal height and 1.6 mm pitch) collimators (^{57}Co source). Several source to collimator distances, denoted by z, were studied.

$$DQE_{Optimized\_collimator}(\nu) \geqslant DQE_{LEHR\_collimator}(\nu) \qquad \forall \nu \in \text{range of interest} \qquad (5)$$

$$DQE_{Optimized\_collimator}(0) \geqslant DQE_{Collimator}(0) \qquad \nabla Collimator. \qquad (6)$$

Comparing the curves in figure 11, we find that the optimized HiSens collimator in terms of DQE has a 1.6 mm collimator pitch and a 21 mm septal height. Its DQE values are greater than the LEHR ones for all frequencies below to 1.03 cm^{-1} and similar for frequencies above 1.03 cm^{-1}. Considering the DQE values at the 0 cm^{-1} frequency, an efficiency gain of about 2 can be expected compared to the LEHR collimator.

Figure 12 compares the DQE curves obtained with the LEHR collimator and the optimized H21 HiSens collimator (21 mm septal height and 1.6 mm pitch) for 5–15 cm source to collimator distances. They show that the characteristics of the collimator described previously are optimized for a large range of source to collimator distances considering 0–1.5 cm^{-1} spatial frequencies.

The contrast against noise curve corresponding to the optimized H21 HiSens collimator (H21 3 virtual layers, with over-pixelization) is plotted in figure 8. It shows that the LEHR performance is correctly recovered thanks to the CZT over-pixelization.

Figure 13 shows GATE-simulated projections of the Derenzo phantom (0.55 Mcounts on each image) obtained with the LEHR, the optimized H21 HiSens and the H13 collimators. They highlight the image deterioration due to the use of a large aperture collimator.

Figure 14 compares Derenzo phantom reconstructed images for two different levels of noise in the reconstructed images, corresponding to different numbers of iterations as the convergence speed depends on the configuration. The GATE projections had the same number of counts. This figure shows the benefit brought by the CZT over-pixelization on the spatial resolution and confirms that the DOI information has no impact for this geometric
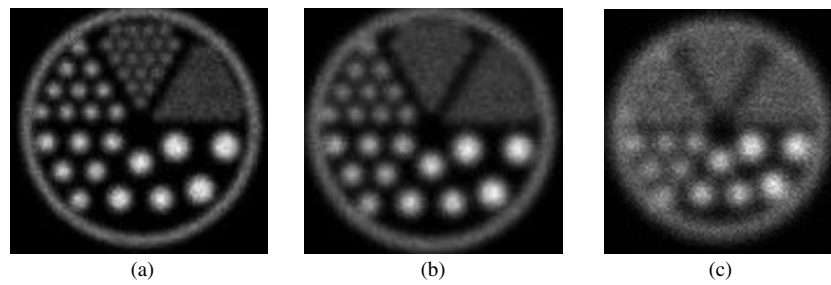
(a)   (b)   (c)

Figure 13. GATE-simulated projections of the Derenzo type phantom (^{57}Co) with (a) the LEHR collimator, (b) the optimized H21 HiSens collimator (without over-pixelization) and (c) the H13 collimator (without over-pixelization).

	H29 LEHR reference	H21 1 virtual layer/ Without over-pixelization	H21 1 virtual layer/ With over-pixelization	H21 3 virtual layers/ With over-pixelization	H13 3 virtual layers/ With over-pixelization
Acquisition duration	1369 s	716 s	716 s	716 s	283 s
	20 iterations – one OSEM subset	100 iterations – one OSEM subset	30 iterations – one OSEM subset	10 iterations – three OSEM subsets	20 iterations – three OSEM subsets
Noise level 1					
	100 iterations – one OSEM subset	400 iterations – one OSEM subset	200 iterations – one OSEM subset	50 iterations – three OSEM subsets	80 iterations – three OSEM subsets
Noise level 2					

Figure 14. Reconstructed images of the Derenzo phantom (^{57}Co) with two different noise levels in the reconstructed images. Row 1 corresponds to a noise level of 0.026 (noise level 1) and row 2 to a noise level of 0.063 (noise level 2). GATE projections had the same count number (0.55 Mcounts). Images are represented using common min. and max. for all images.

configuration in planar imaging. The comparison with the LEHR collimator shows that the optimized H21 HiSens architecture (H21 3 virtual layers/with over-pixellization) recovers the spatial resolution lost by the large collimator aperture of the optimized H21 HiSens collimator while reducing acquisition duration by 2.

4.4. Simulation-based evaluation of the HiSens architecture in SPECT

Figure 15 compares the simulated reconstructed images through the hot spheres of the cylindrical phantom with the same level of noise, i.e. the same level of convergence, for the LEHR, the optimized H21 HiSens and the H13 collimators. For the H13 collimator (columns
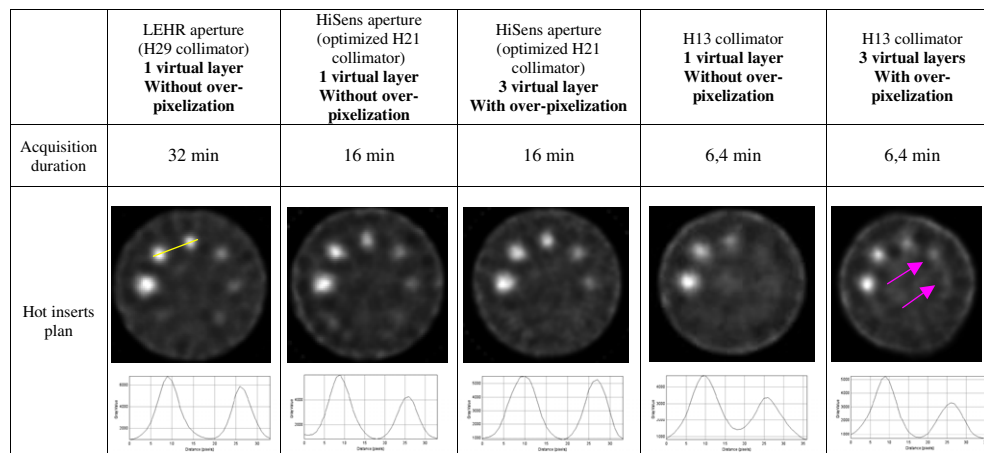
	LEHR aperture (H29 collimator) **1 virtual layer Without over-pixelization**	HiSens aperture (optimized H21 collimator) **1 virtual layer Without over-pixelization**	HiSens aperture (optimized H21 collimator) **3 virtual layer With over-pixelization**	H13 collimator **1 virtual layer Without over-pixelization**	H13 collimator **3 virtual layers With over-pixelization**
Acquisition duration	32 min	16 min	16 min	6,4 min	6,4 min
Hot inserts plan					

Figure 15. Reconstructed images (hot inserts) of the cylindrical phantom (^{99m}Tc source) with the same noise level using the LEHR, the optimized H21 HiSens and the H13 collimators. GATE-simulated projections had 0.3 Mcounts/view angle. Images are represented using common min. and max. for all images.

Table 1. Contrast values measured on the reconstructed images for the different hot inserts.

	LEHR aperture (H29 collimator) 1 virtual layer without over-pixelization	HiSens aperture (optimized H21 collimator) 1 virtual layer without over-pixelization	HiSens aperture (optimized H21 collimator) 3 virtual layers with over-pixelization	H13 collimator 1 virtual layer without over-pixelization	H13 collimator 3 virtual layers with over-pixelization
Insert 1 (19.2 mm)	71.8%	72.1%	71.8%	62.4%	62.2%
Insert 2 (16.0 mm)	71.0%	70.9%	66.3%	50.2%	54.6%
Insert 3 (12.8 mm)	66.7%	60.6%	64.9%	36.3%	38.4%
Insert 4 (9.6 mm)	47.5%	47.5%	50.1%	4.6%	28.8%
Insert 5 (8.0 mm)	36.0%	39.5%	43.1%	6.1%	10.6%

4 and 5), the accurate localization of the interactions along the *x*- and *y*-axes introduced by the detector over-pixelization improves the spatial resolution (see profiles) and the contrast. For example, the contrast of the second largest hot insert is increased from 50% to 55% (table 1) thanks to the HiSens processing. Moreover, the 9.6 mm and 8.0 mm hot inserts, which were not visible in the reconstructed image without over-pixelization become visible with over-pixelization (pink arrows). However, as in planar imaging, we can clearly conclude that the H13 collimator does not fulfil our optimization criterion. For the optimized H21 HiSens collimator (columns 2 and 3), the merits of the HiSens architecture are confirmed: the contrast is improved for the smallest inserts (table 1). Finally, the optimized H21 HiSens collimator reconstructed image corresponding to the 3 DOI with over-pixelization configuration is very similar to that obtained using the LEHR collimator. Only the 6.4 mm hot insert is better defined with the LEHR collimator than that with the optimized H21 HiSens collimator.

Figure 16 compares the simulated reconstructed images through the cold spheres of the cylindrical phantom with the same level of noise for the LEHR and the optimized H21 HiSens
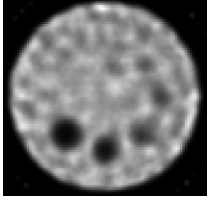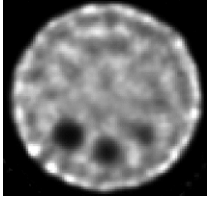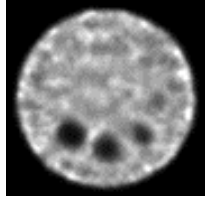
	LEHR aperture (H29 collimator) **1 virtual layer Without over-pixelization**	HiSens aperture (optimized H21collimator) **1 virtual layer Without over-pixelization**	HiSens aperture (optimized H21collimator) **3 virtual layer With over-pixelization**
Acquisition duration	32 min	16 min	16 min
Cold inserts plan			

Figure 16. Reconstructed images (cold inserts) of the cylindrical phantom (^{99m}Tc source) with the same noise level using the LEHR and the optimized H21 HiSens collimators. GATE projections had 0.3 Mcounts/view angle. Images are represented using common min. and max. for all images.

Table 2. Contrast values measured in the reconstructed images for the 19.2/16.0 and 12.8 mm cold inserts.

	LEHR aperture (H29 collimator) 1 virtual layer without over-pixelization	HiSens aperture (optimized H21 collimator) 1 virtual layer without over-pixelization	HiSens aperture (optimized H21 collimator) 3 virtual layers with over-pixelization
Insert 1 (19.2 mm)	90.0%	85.0%	86.2%
Insert 2 (16.0 mm)	78.7%	71.6%	75.0%
Insert 3 (12.8 mm)	47.6%	46.5%	56.5%

collimators. Contrast measurements (table 2) show that the HiSens architecture improves the contrast of the cold inserts. For example, for the 12.8 mm insert, the contrast is increased from 46% to 56% with the optimized H21 HiSens collimator thanks to the HiSens processing.

5. Discussion

In this work, we used simulations and experiments to assess the performance of an original so-called HiSens detector architecture, based on finely sampled CZT detectors and DOI information.

Two simulation software packages were used in our study. GATE was used to simulate all projections used to characterize the image features obtained using the HiSens imaging device. These projections were affected by Compton and Rayleigh scatter, and a simple model for the electronic detector response was used. By comparing simulated and real images obtained from an experimental set-up, we first checked that our simulation model with GATE produced images similar to those acquired with the real acquisition device.

The SINDBAD software using ray tracing (thus ignoring Compton and Rayleigh scatter) was used in two instances: to produce the data used to calculate the DQE curves and for
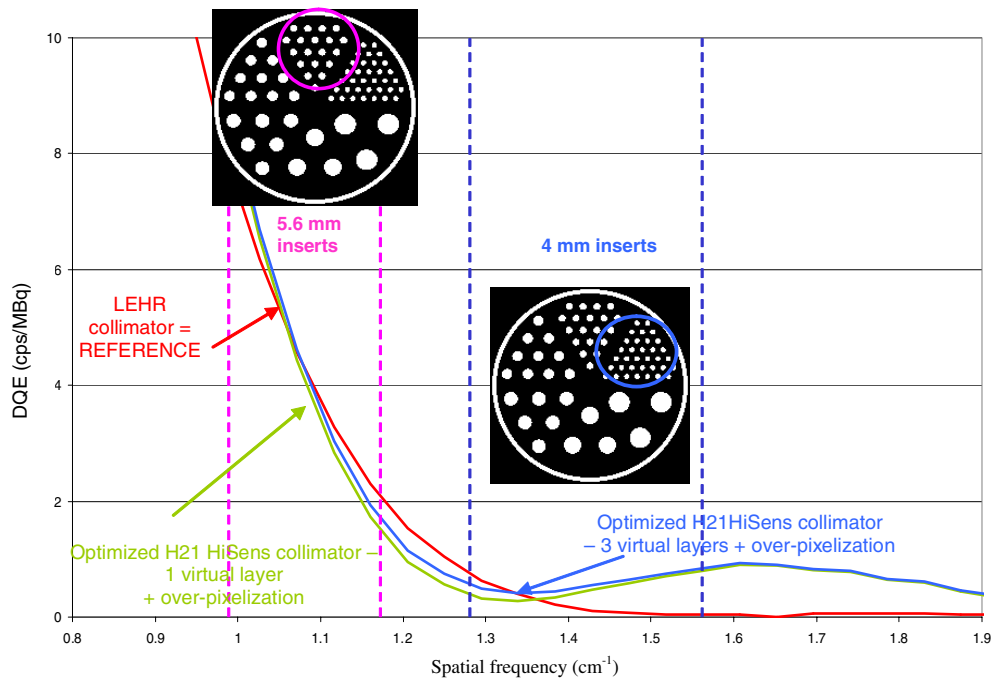
Figure 17. Zoom on the DQE curves (^{57}Co source) obtained with the LEHR and the optimized H21 HiSens collimators (with 1 and 3 virtual layers). Positions of the Derenzo inserts of interest are shown to explain the resolution recovery seen in the reconstructed images.

the efficient calculation of most of the system matrices needed to obtain the images from the detected signal. The fact that projections produced with GATE were properly reconstructed using a system matrix calculated with SINDBAD shows that reliable images can be obtained using HiSens even when using approximate system matrices. Our results also suggest that the results obtained using realistic projections obtained with GATE were consistent with the predictions made using the DQE curves based on SINDBAD simulations.

Using the simulations, we first showed that the contribution of the DOI information is actually limited: the HiSens interest mainly lies in the fine CZT detector pixelization under the geometrical conditions considered here.

Using our simulation model, we varied the collimator parameters to determine which collimator would make the most of the HiSens architecture. This analysis was based on a DQE study. The DQE analysis suggested that for a 100 mm source–collimator distance, the collimator that would at least recover or even improve the LEHR collimator spatial resolution with a maximum gain in efficiency should have a 21 mm septal height and a 1.6 mm pitch considering 0.8 mm × 0.8 mm detector virtual pixels which corresponds to 4 pixels per collimator hole. Images of the Derenzo phantom (figure 14) confirmed that this optimized H21 HiSens collimator (in terms of the DQE curves) led to images similar to those obtained with the LEHR collimator, or even with improved spatial resolution (see the 4 mm inserts). This is because the 4 mm inserts correspond to frequencies of about 1.3–1.6 cm^{-1}, which is a frequency range for which the DQE values obtained with the optimized H21 HiSens collimator are greater than those obtained with the LEHR collimator (figure 17). On the other hand, for the 5.6 mm inserts which correspond to frequencies of about 1–1.2 cm^{-1}, the DQE values are
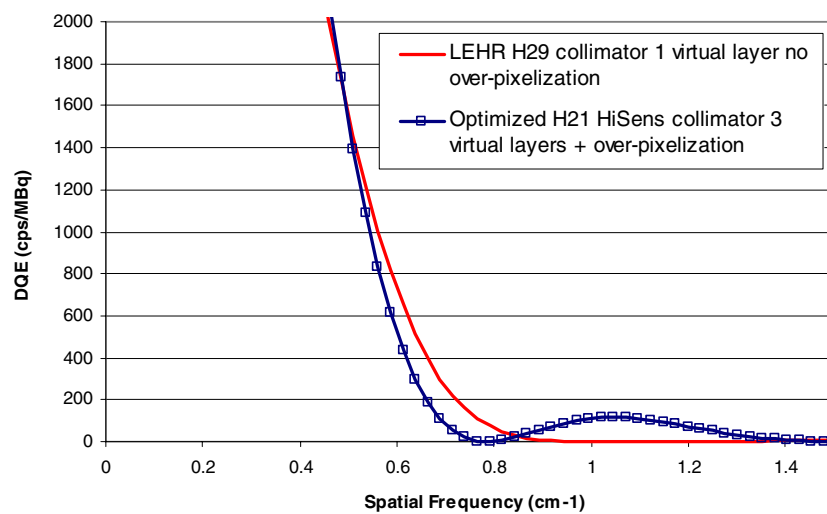
Figure 18. DQE curves obtained with the LEHR and the optimized H21 HiSens (three virtual layers + over-pixelization) collimators for a 164 mm source to collimator distance (planar acquisition mode)—a ^{99m}Tc point source was considered.

nearly the same for the LEHR and the optimized H21 HiSens collimators, which explains that the inserts are recovered similarly in the reconstructed images (figure 14).

Based on this study, we can thus conclude that the HiSens architecture, combined with an appropriate collimation, can improve (in our case by a factor of 2) the detection efficiency and therefore decrease the acquisition duration while equaling or improving the image spatial resolution.

In SPECT, both reconstructed images and contrast measurements showed that the HiSens architecture can improve the image characteristics when a high aperture collimator is associated with the high resolution detector. Figure 15 showed that the image corresponding to the optimized H21 collimator associated with the HiSens architecture (three virtual layers + over-pixelization) is comparable to the reference LEHR collimator one. However, the 6.4 mm inserts were better defined with the H29 collimator. This observation is consistent with the DQE curves corresponding to a 164 mm source to collimator distance (radius of rotation), measured in planar mode (figure 18). Indeed, for this source to collimator distance, the DQE values of the optimized H21 HiSens collimator (three virtual layers + over-pixelization) are lower than the LEHR collimator ones for a large frequency band (0.5–0.85 cm^{-1}), which can explain why some inserts are better defined with the LEHR than with the optimized H21 HiSens collimator.

Considering the geometry of the simulated phantom, only contrast and noise figures of merit could be evaluated. DQE measurements including the spatial frequency notion help to characterize a detection system response. The development of a DQE program appropriate for collimation optimization in SPECT is thus in progress.

In planar and SPECT acquisition modes, DQE was evaluated considering a uniform background (section 3.3.1). However, image recovery also depends on the source characteristics (e.g. hot or cold spots). A DQE-like figure of merit that also depends on the object features is currently under development to overcome this limitation of the standard DQE.

Finally, a complete characterization of the absolute performance of the HiSens architecture will require a more realistic modelling of the electronic response of the detector.

6. Conclusion

The HiSens architecture combines a high sensitivity parallel hole collimator to a high resolution CZT detector. An electronically based 3D positioning algorithm makes it possible to use DOI information and over-pixelization (i.e. several virtual pixels per collimator hole) without increasing the number of readout channels. We showed that the over-pixelization was actually the feature that most improved the achievable trade-off between spatial resolution and sensitivity in the HiSens architecture.

In planar mode, we showed that accurate collimator deconvolution, performed using an adapted OSEM algorithm, improves the reconstructed image. A DQE analysis showed that for a 100 mm source–collimator distance, a twofold increase in sensitivity can be achieved using the HiSens architecture without compromising contrast recovery and spatial resolution, suggesting that the acquisition duration can be reduced by 2.

Preliminary results in SPECT suggest that the HiSens architecture can also improve the image characteristics in tomographic mode. However, the non-stationary resolution recovery in the reconstructed image needs to be accounted for in the DQE analysis. A generalization of the DQE analysis tool in 3D is in progress for optimizing the collimator/detector/processing parameters for SPECT acquisitions.

Acknowledgment

References

Anger H O 1967 Radioisotope camera *Instrumentation in Nuclear Medicine* vol 1, ed G J Hine (New York: Academic) chapter 19
Barber H B 1999 Applications of semiconductor detectors to nuclear medicine *Nucl. Instrum. Methods* A **436** 102–10
Cunningham I A and Shaw R 1999 Signal-to-noise optimization of medical imaging systems *J. Opt. Soc. Am.* A **16** 621–32
Eisen Y 1996 Current state-of-art industrial and research applications using room-temperature CdTe and CdZnTe solid state detectors *Nucl. Instrum. Methods* A **380** 431–9
Eisen Y, Mardor I and Shor A 2002 NUCAM3 a gamma camera based on segmented monolithic CdZnTe detectors *IEEE Trans. Nucl. Sci.* **49** 1728–32
Gros D'Aillon E, Gentet M C, Montémont G and Verger L 2005 Simulation and experimental results on monolithic CdZnTe gamma-ray detectors *IEEE Trans. Nucl. Sci.* **32** 3096–102
Guérin L, Verger L, Rebuffel V and Monnet O 2008 A new architecture for pixellated solid state gamma camera used in nuclear medicine *IEEE Trans. Nucl. Sci.* **55** 1573–80
He Z, Knoll G F, Wehe D K, Rojeski R, Mastrangelo C H, Hammig M, Barrett C and Uritani A 1996 1 D position sensitive single carrier semiconductor detector *Nucl. Instrum. Methods* A **380** 228–31
Hudson H M and Larkin R S 1994 Accelerated image-reconstruction using ordered subsets of projection data *IEEE Trans. Med. Imaging* **13** 601–9
Jan S *et al* 2004 GATE: a simulation toolkit for PET and SPECT *Phys. Med. Biol.* **49** 4543–61
Montémont G, Bordy T, Rebuffel V, Robert C and Verger L 2008 CZT pixel detectors for improved SPECT imaging *IEEE Nuclear Science Symp. Conf. Record* pp 84–9
Scheiber C and Giakos G C 2001 Medical applications of CdTe and CdZnTe detectors *Nucl. Instrum. Methods* A **458** 12–25

Starck S, Bath M and Carlsson S 2005 The use of detective quantum efficiency (DQE) in evaluating the performance of gamma camera systems *Phys. Med. Biol.* **50** 1601–9

Tabary J, Guillemaud R and Mathy F 2004 Combination of high resolution analytically computed uncollided flux images with low resolution Monte Carlo computed scattered flux images *IEEE Trans. Nucl. Sci.* **51** 212–7

Verger L, Bonnefoy J P, Glasser F and Ouvrier-Buffet P 1997 New developments in CdTe and CdZnTe detectors for x and gamma-ray applications *J. Electron. Mater.* **26** 738–44

Verger L, Gentet M C, Guillemaud R, Mestais C, Monnet O, Montémont G, Petroz G, Rostaing J P and Rustique J 2004 Performance and perspectives of a CdZnTe based gamma camera for medical imaging *IEEE Trans. Nucl. Sci.* **51** 3111–7

Wagenaar D J, Chowdhury S, Engdahl J C and Burckhardt D D 2003 Planar image quality comparison between a CdZnTe prototype and a standard NaI(Tl) gamma camera *Nucl. Instrum Methods* A **505** 586–9

Warburton W K 1997 An approach to sub-pixel spatial resolution in room temperature x-ray detector arrays with good energy resolution *Semiconductors for Room-Temperature Radiation Detector Applications II, Materials Research Society Symp. Proc.* pp 531–5